Characterization and Application of Nanomaterials 2026, 9(1), 026100005.
https://doi.org/10.24294/can026100005

Article

Defect-mediated Electrical transport and photoluminescence correlation in nanostructured Fe_3O_4 synthesized via controlled co-precipitation

Dipti Shukla

Department of Physics, O P Jindal University, Raigarh, Chhattisgarh 496001, India, dipti.shukla@opju.ac.in

CITATION

Shukla D. Defect-mediated Electrical transport and photoluminescence correlation in nanostructured Fe_3O_4 synthesized via controlled co-precipitation. Characterization and Application of Nanomaterials. 2026; 9(1): 026100005. https://doi.org/10.24294/can026100005

ARTICLE INFO

Received: 08 March 2026
Accepted: 21 April 2026
Available online: 22 May 2026

Abstract: Magnetite (Fe_3O_4) nanoparticles exhibit complex charge transport behavior governed by mixed-valence electronic structure and defect chemistry. In this study, Fe_3O_4 nanoparticles were synthesized via a controlled co-precipitation method under an inert atmosphere to preserve Fe^{2+} states and suppress secondary phase formation. X-ray diffraction confirms the formation of a nanocrystalline inverse spinel structure with an average crystallite size of ~16 nm. Morphological analysis reveals quasi-spherical, agglomerated nanoparticles. Photoluminescence spectra exhibit distinct emission bands in the visible and near-infrared regions, attributed to defect-mediated recombination involving oxygen vacancies and localized states. Temperature-dependent electrical measurements reveal non-linear semiconducting behavior with an anomalous decrease in resistivity in the 283–293 K range. This behavior is attributed to defect-assisted percolative conduction and thermally activated small polaron hopping rather than any intrinsic phase transition. The study establishes a direct correlation between defect-induced optical states and electrical transport mechanisms. The findings provide important insights into defect-engineered transport phenomena in Fe_3O_4 nanostructures for potential applications in sensing and electronic devices.

Keywords: Fe_3O_4 nanoparticles; defect states; small polaron hopping; photoluminescence; electrical transport; grain boundary conduction; nanostructured oxides

1. Introduction

Magnetite (Fe_3O_4) is a prototypical mixed-valence transition metal oxide known for its coupled electrical, magnetic, and structural properties. It crystallizes in an inverse spinel structure (space group $Fd\bar{3}m$), where Fe^{3+} ions occupy tetrahedral (A) sites, while Fe^{2+}/Fe^{3+} ions reside at octahedral (B) sites. This mixed-valence configuration enables electron hopping between Fe^{2+} and Fe^{3+}, giving rise to its characteristic electrical conductivity and making Fe_3O_4 a model system for charge transport in correlated oxides [1–5]. In bulk Fe_3O_4, the well-known Verwey transition (~120 K) is associated with charge ordering and a metal– insulator transition. However, at the nanoscale, this behavior is significantly altered due to size confinement, lattice strain, and defect formation, which introduce localized electronic states and modify both optical and electrical responses. Nanostructured Fe_3O_4 has attracted considerable interest for applications in sensing, catalysis, biomedicine, and electronic devices. In such systems, electrical transport is governed by a combination of mechanisms, including small polaron hopping, grain boundary effects, interparticle tunneling, and defect- mediated conduction. These processes are highly sensitive to microstructural parameters such as particle size, morphology, and defect density [6]. Defect states, particularly oxygen vacancies and surface trap centers, play a central role in determining functional properties. Photoluminescence (PL) spectroscopy serves as an effective tool for probing these defect states, while electrical measurements provide

insight into their influence on charge transport. However, a direct correlation between defect-induced optical emissions and electrical conduction in Fe_3O_4 nanoparticles remains insufficiently explored [7]. Additionally, anomalous resistivity variations observed near room temperature in nanostructured oxides are often ambiguously interpreted, sometimes being incorrectly attributed to phase transitions. In reality, such behavior frequently arises from extrinsic effects such as grain boundary conduction and defect-assisted percolation, necessitating careful analysis of transport mechanisms.

In this context, the present study investigates Fe_3O_4 nanoparticles synthesized via controlled co-precipitation, with emphasis on correlating structural features, defect states, and electrical transport behavior. A comprehensive characterization approach combining XRD, SEM, photoluminescence, and temperature-dependent resistivity measurements is employed to elucidate defect-mediated conduction mechanisms [8–10].

The key novelty of this work lies in demonstrating that the observed resistivity reduction near room temperature (283–293 K) originates from defect-assisted percolative conduction rather than any intrinsic phase transition. Furthermore, a direct correlation between photoluminescence-derived defect states and electrical transport is established, providing a unified framework for understanding charge conduction in nanostructured Fe_3O_4.

2. Materials and methods

2.1. Synthesis of Fe_3O_4 nanoparticles

Fe_3O_4 nanoparticles were synthesized via a controlled chemical co-precipitation route under an inert atmosphere to minimize oxidation of Fe^{2+} ions. Analytical-grade ferric chloride ($FeCl_2$) and ferrous precursor (Mohr's salt, $(NH_4)_2Fe(SO_4)_2 \cdot 6H_2O$) were employed as iron sources. Specifically, 1.19 g of $FeCl_3$ and 0.95 g of Mohr's salt were dissolved in 50 mL of deoxygenated double-distilled water under continuous nitrogen purging. A stoichiometric Fe^{2+}:Fe^{3+} molar ratio of 1:2 was maintained, with an additional ~10% excess of Fe^{2+} precursor to compensate for possible oxidation during synthesis [11,12].

A 25 mL aliquot of 1 M NaOH solution, pre-deoxygenated under nitrogen, was rapidly introduced into the reaction mixture while maintaining the temperature at 80 °C under vigorous magnetic stirring. The reaction was allowed to proceed for 15 min under a continuous nitrogen atmosphere, followed by controlled cooling to room temperature over ~1 h.

The resulting black precipitate, characteristic of magnetite, was magnetically separated, repeatedly washed with deionized water until a neutral pH was achieved, and subsequently dried under a nitrogen environment to prevent surface oxidation [13]. The overall reaction can be represented as:

$$Fe^{2+} + 2Fe^{3+} + 8OH^- \rightarrow Fe_3O_4 + 4H_2O$$

2.2. X-ray diffraction (XRD) analysis (including Williamson–Hall method)

The crystallographic structure and phase composition of the synthesized Fe_3O_4 nanoparticles were analyzed using a Bruker D8 Advance X-ray diffractometer with Cu Kα radiation (λ = 0.15406 nm), operated at 40 kV and 20 mA. Diffraction patterns were recorded over a 2θ range of 20–70°.

The average crystallite size (D) was initially estimated using the Debye–Scherrer equation. However, since peak broadening in XRD patterns arises from both finite crystallite size and lattice strain, a more comprehensive analysis was performed using the Williamson–Hall (W–H) method based on the uniform deformation model (UDM).

The Williamson–Hall equation is expressed as [13]:

$$\beta\cos\theta = K\lambda/D + 4\varepsilon\sin\theta$$

where:

- β is the full width at half maximum (FWHM) corrected for instrumental broadening,
- θ is the Bragg angle,
- K is the shape factor (0.9),
- λ is the X-ray wavelength,
- D is the crystallite size, and
- ε represents the lattice strain.

A plot of βcosθ versus 4sinθ was constructed, and a linear fit was applied. The intercept of the fitted line corresponds to Kλ/D, from which the crystallite size was calculated, while the slope provides the rate of lattice strain (ε).

This method allows for the separation of size-induced and strain-induced broadening effects, providing a more reliable estimation of microstructural parameters compared to the Scherrer approach alone. The observed strain is attributed to lattice distortions, surface tension, and defect states inherent in nanoscale Fe_3O_4 particles.

2.3. Scanning electron microscopy (SEM) and elemental analysis

The surface morphology and microstructural features of the synthesized Fe_3O_4 nanoparticles were investigated using a field-emission scanning electron microscope (FESEM, QUANTA-200F, FEI, Hillsboro, OR, USA).

Imaging was performed at suitable accelerating voltages and magnifications to resolve particle size, surface texture, and agglomeration behaviour [14].

Energy-dispersive X-ray spectroscopy (EDS), attached to the SEM system, was employed to qualitatively confirm the elemental composition and purity of the samples. The observed morphology is interpreted considering interparticle magnetic interactions and surface energy effects, which commonly lead to agglomeration in magnetic nanoparticle systems.

2.4. Photoluminescence (PL) spectroscopy

Photoluminescence measurements were carried out using a Hitachi RF-5301PC spectrofluorophotometer (Tokyo, Japan) under ambient conditions. The powdered sample was excited at a wavelength of 325 nm, and emission spectra were recorded

over the visible to near-infrared spectral range [15].

The emission features were analyzed in terms of defect-mediated electronic transitions, including oxygen vacancy states, Fe^{2+}–Fe^{3+} charge transfer processes, and surface-related trap states. These optical characteristics provide insight into the electronic structure and defect landscape of the nanoparticles, which are also relevant to their electrical transport behavior.

2.5. Electrical measurement methodology

Electrical resistivity measurements were carried out on pelletized samples prepared from the synthesized Fe_3O_4 nanopowder. The powder was compacted into circular pellets using a uniaxial hydraulic press under an applied pressure of approximately 5 tons. The resulting pellets exhibited an average diameter of ~10 mm and a thickness in the range of ~1–2 mm, ensuring adequate mechanical stability and uniform geometry for electrical measurements. The schematic representation of the experimental setup used for electrical resistivity measurements is shown in **Figure 1**.

For electrode fabrication, a uniform layer of conductive silver paste was applied to both flat surfaces of the pellets to establish electrical contacts. The coated pellets were subsequently dried at a moderate temperature to ensure proper adhesion and formation of stable ohmic contacts, thereby minimizing interfacial resistance. Ohmic behavior of the contacts was verified before measurements.

Electrical measurements were performed using a two-probe configuration with a Keithley 2400 Source Meter (Solon, OH, USA), operated in constant voltage mode. A controlled voltage in the range of 1–5 V was applied across the sample, and the resulting current was recorded to determine the resistivity. The applied voltage was carefully optimized to avoid Joule heating and ensure stable measurement conditions.

All measurements were conducted in ambient air under laboratory humidity conditions over a temperature range of 273–310 K. The temperature was varied at a controlled heating rate of approximately 2 K/min, and data were collected during both heating and cooling cycles to verify reproducibility.

Repeated measurements were performed to ensure consistency, yielding an experimental uncertainty of approximately ±3%. Care was taken to maintain stable contact conditions throughout the measurements to reduce fluctuations arising from contact resistance and thermal drift.

It is important to emphasize that the two-probe technique inherently includes contributions from contact resistance and electrode–sample interface effects. As a result, this method does not provide absolute resistivity values but is suitable for analyzing relative temperature- dependent trends in electrical behavior. Furthermore, the two-probe configuration cannot resolve true zero-resistance states; therefore, it is not appropriate for confirming superconductivity. Consequently, the observed decrease in resistivity is interpreted in terms of defect-assisted conduction mechanisms rather than any superconducting transition.

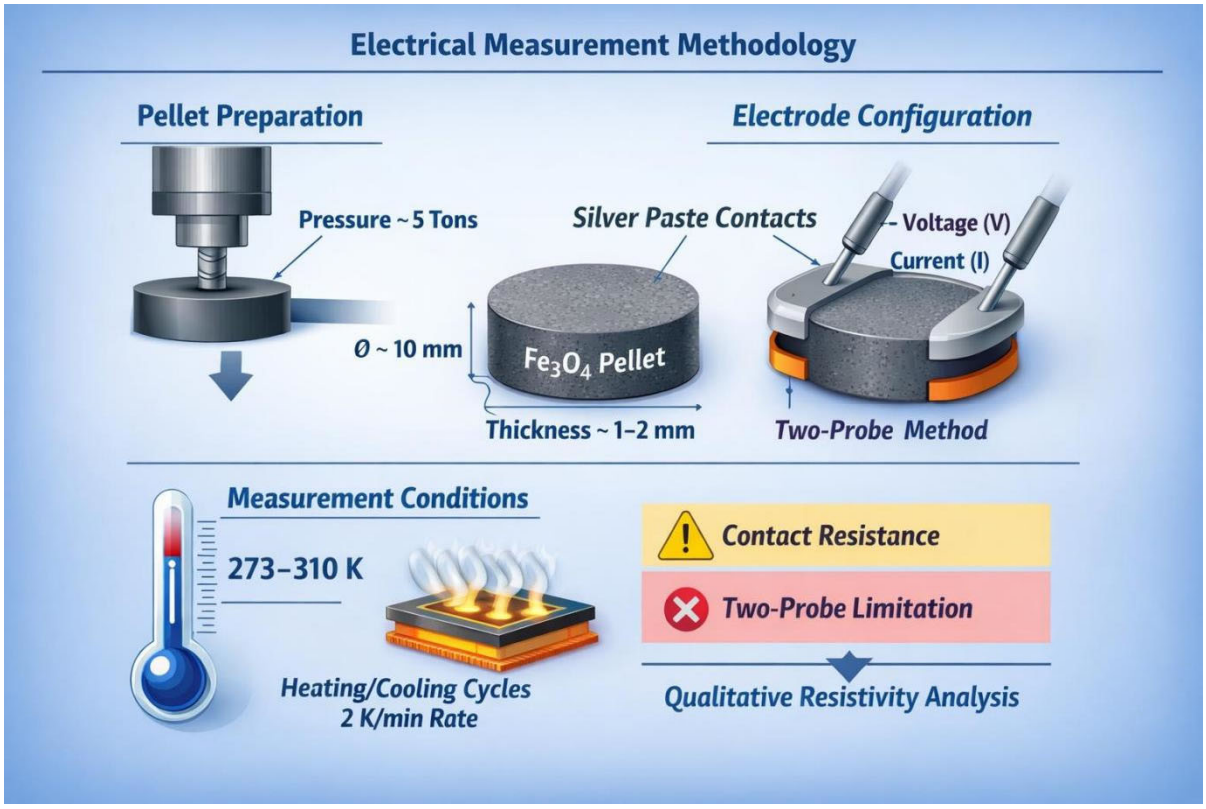

Figure 1. Schematic illustration of the electrical measurement methodology for Fe_3O_4 nanoparticles. The nanopowder is first compacted into pellets using a uniaxial hydraulic press under an applied pressure of ~5 tons, resulting in pellets with a diameter of ~10 mm and a thickness of ~1–2 mm.

3. Results and discussion

3.1. Structural analysis via X-ray diffraction (XRD)

The X-ray diffraction (XRD) pattern is consistent with the formation of a cubic inverse spinel structure corresponding to Fe_3O_4 (JCPDS standard data) [16]. However, it is well established that XRD alone cannot unambiguously distinguish between magnetite (Fe_3O_4) and maghemite (γ-Fe_2O_3), particularly in nanostructured systems due to their closely similar diffraction profiles (**Figure 2a,b**). The prominent reflection at $2\theta \approx 35.08°$ is indexed to the (311) plane, accompanied by characteristic peaks at 30.28°, 43.24°, 53.60°, and 63.04°, corresponding to the (220), (400), (422), and (440) planes, respectively. No additional peaks corresponding to secondary crystalline phases are observed within the detection limits of the instrument.

Therefore, while the observed diffraction pattern strongly supports the presence of Fe_3O_4, the possibility of partial surface oxidation leading to γ-Fe_2O_3 cannot be completely excluded. The absence of impurity peaks suggests phase purity within the resolution limits of XRD; however, complementary techniques would be required for definitive phase discrimination.

Williamson–Hall analysis (**Figure 2c**) reveals the presence of moderate lattice strain, which can be attributed to nanoscale size effects, surface stress, and defect-induced lattice distortions. The extracted structural parameters are in good agreement with previously reported values for nanostructured Fe_3O_4. The structural parameters

obtained from X-ray diffraction analysis, including diffraction angle (2θ), Miller indices (hkl), interplanar spacing (d), crystallite size (D), lattice parameter (a), full width at half maximum (FWHM), and crystallinity degree, are summarized in **Table 1**. These parameters confirm the formation of crystalline cubic spinel Fe_3O_4 nanoparticles and provide detailed insight into their phase purity and microstructural characteristics.

For quantitative structural evaluation, the X-ray diffraction patterns of the synthesized Fe_3O_4 nanoparticles were subjected to Rietveld refinement using a cubic inverse spinel structure (space group $Fd\bar{3}m$), consistent with standard JCPDS data [16]. The refinement profiles (**Figure 2**) exhibit good agreement between the observed and calculated patterns, indicating the reliability of the structural model within the limits of XRD analysis.

The refined lattice parameter was found to be approximately a = 8.39 Å, yielding a unit cell volume of 593.6 $Å^3$, which is in good agreement with reported values for nanostructured Fe_3O_4. The refinement quality indicators, including weighted profile factor (Rwp = 9.8%), expected R-factor (Rexp = 8.23%), and goodness-of-fit parameter ($\chi^2 = 1.42$), demonstrate a satisfactory agreement between the observed and calculated diffraction profiles, confirming the reliability of the structural model. The refinement reliability factors (Rwp, Rp, Rexp) and goodness-of-fit (χ^2) confirming satisfactory agreement between the observed and calculated diffraction profiles are summarized in **Table 2**, validating the formation of the cubic inverse spinel Fe_3O_4 phase within the limits of analysis.

It is noted that, although the refinement supports the predominance of the Fe_3O_4 phase, XRD alone cannot unambiguously distinguish between Fe_3O_4 and γ-Fe_2O_3 due to their similar crystallographic features. Therefore, minor contributions from surface oxidation cannot be completely excluded. Overall, the results demonstrate that the synthesized nanoparticles possess a well-defined inverse spinel structure with slight lattice distortions arising from nanoscale effects and defect states.

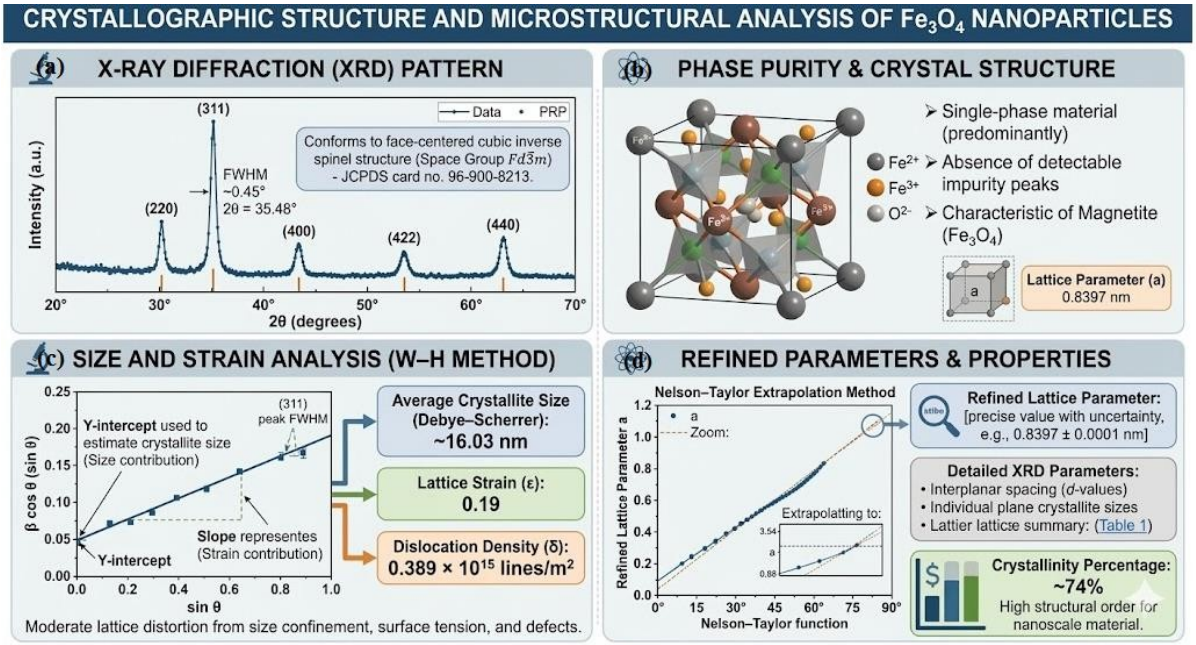

Figure 2. Comprehensive Crystallographic and Microstructural Analysis of Synthesized Fe3O4 Nanoparticles. (**a**) XRD Diffraction Pattern: Recorded in the 2θ range of 20° –70), (**b**) Crystal Structure Model, (**c**) Williamson–Hall (W–H) plot used to separate size-induced broadening from lattice strain, indicating the presence of moderate microstrain associated with nanoscale effects and defect states. (**d**) Rietveld refinement profile showing the observed data.

Table 1. Structural parameters of Fe_3O_4 nanoparticles obtained from XRD analysis, including diffraction angle (2θ), Miller indices (hkl), interplanar spacing (d), crystallite size (D), lattice parameter (a), and full width at half maximum (FWHM). These parameters provide insight into the phase purity, crystallinity, and microstructural characteristics of the synthesized nanoparticles.

Phase	Miller Indices hkl	2θ degree	Interplane spacing d A^0	L nm	Cell Parameter α nm	FWHM	Crystallinity degree, %
	111	18.2^0	4.885	11.31	0.835	0.792	74%
	220	30.28^0	2.946	13.83		0.663	
	311	35.08^0	2.512	13.65		0.681	
Fe_3O_4	222	37.24^0	2.413	30.99		0.302	
	400	43.24^0	2.093	12.97		0.734	
	422	53.6^0	1.717	16.38		0.604	
	511	57.23	1.628	15.47		0.657	
	440	63.04^0	1.485	13.05		0.795	

Using the required number of symmetric pseudo-Voigt functions to approximate the diffractogram's lines, the full width at half maximum (FWHM) was computed. It enabled us to assess the degree of crystallinity and characterise the quality of the crystal structure. After the treatment, it was discovered that the initial sample's crystallinity degree was 74%.

Table 2. The refinement reliability factors (Rwp, Rp, Rexp) and goodness-of-fit (χ^2) confirm a satisfactory agreement between the observed and calculated diffraction profiles, validating the formation of the cubic inverse spinel Fe_3O_4 phase within the limits of analysis.

Parameters	Value
Rwp (Weighted profile factor)	9.8%
Rp (Profile factor)	7.5%
Rexp (Expected factor)	8.23%
χ^2 (Goodness of fit)	1.42

3.2. Surface morphology using scanning electron microscope (SEM)

SEM analysis (**Figure 3**) reveals that the synthesized Fe_3O_4 nanoparticles are predominantly quasi-spherical in morphology with a tendency to form agglomerated clusters due to magnetic dipole–dipole interactions and high surface energy. The particle size ranges from approximately 8–25 nm, consistent with XRD results. The surface appears relatively smooth at the nanoscale, with no evidence of large irregular grains or secondary phases. The observed morphology is therefore described as quasi-spherical, agglomerated nanostructures, which is typical for magnetic nanoparticles synthesized via co-precipitation methods [17,18].

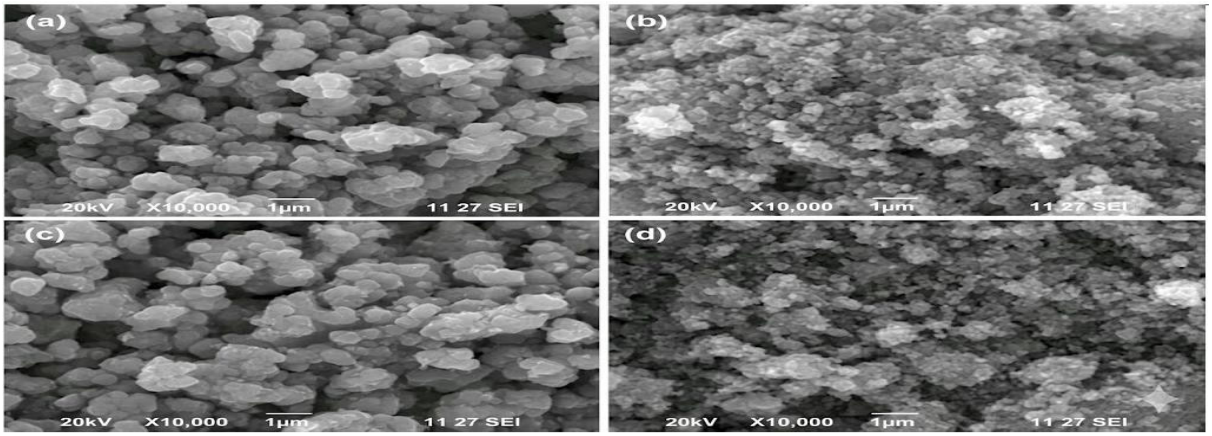

Figure 3. SEM Micrographs of Synthesized Fe_3O_4 Nanoparticles, (**a** and **c**) Surface Morphology: Low-magnification. (**b** and **d**) Detailed Particle Distribution: Higher-resolution views.

3.3. Optical properties

The photoluminescence spectrum of Fe_3O_4 nanoparticles (**Figure 4**) exhibits distinct emission bands centered at ~550 nm, ~698 nm, and ~808 nm, indicating the presence of multiple defect-related electronic transitions [19]. The green emission (~550 nm) is attributed to Fe^{2+}– Fe^{3+} charge transfer transitions within the octahedral sites of the spinel structure. The red emission (~698 nm) originates from oxygen vacancy–related defect states, while the near- infrared emission (~808 nm) is associated with deep-level trap states arising from structural disorder and surface defects.

These emissions confirm the existence of localized electronic states within the band structure, which facilitate radiative recombination processes. More importantly, these defect states act as trapping and hopping centers for charge carriers, thereby playing a crucial role in governing the electrical transport behavior.

A direct correlation between photoluminescence-derived defect states and electrical conduction mechanisms is thus established. The presence of shallow, intermediate, and deep- level defects support a defect-mediated transport model involving thermally activated hopping and percolative conduction pathways.

This integrated interpretation moves beyond descriptive analysis and provides a unified understanding of the structure–property relationship in Fe_3O_4 nanoparticles. The results highlight the significance of defect engineering in tuning both optical and electrical properties, suggesting potential applications in optoelectronic devices, sensing systems, and photothermal technologies [20].

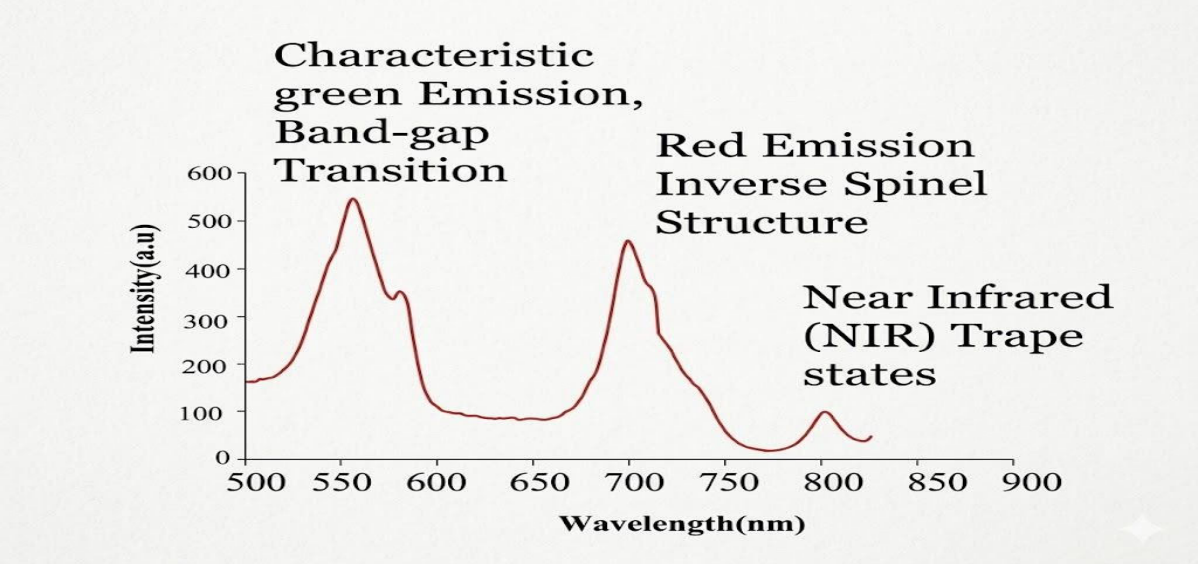

Figure 4. Room-temperature photoluminescence (PL) spectrum of as-synthesized Fe_3O_4 nanoparticles. The spectrum exhibits prominent emission bands centered at ~560 nm, ~700 nm, and ~805 nm, corresponding to characteristic green emission attributed to band-gap transitions, red emission associated with the inverse spinel structure, and near-infrared (NIR) emission arising from defect-related trap states, respectively.

Optical band gap and defect state analysis

To further understand the electronic structure, the optical band gap of the synthesized Fe_3O_4 nanoparticles can be correlated with defect-induced states observed in photoluminescence spectra (**Figure 5**). In nanostructured oxides, the presence of oxygen vacancies and surface defects introduces localized energy levels within the band gap, resulting in sub-bandgap emissions [21].

The observed emission bands at ~550 nm, ~698 nm, and ~808 nm suggest the presence of shallow, intermediate, and deep-level defect states, respectively. These defect levels facilitate radiative recombination and also act as trapping centers, influencing charge transport.

The coexistence of these defect states supports the electrical transport mechanism, where carriers hop via localized states rather than extended band conduction. This establishes a direct link between optical emissions and electrical conductivity,

reinforcing the defect- mediated transport model proposed in this study.

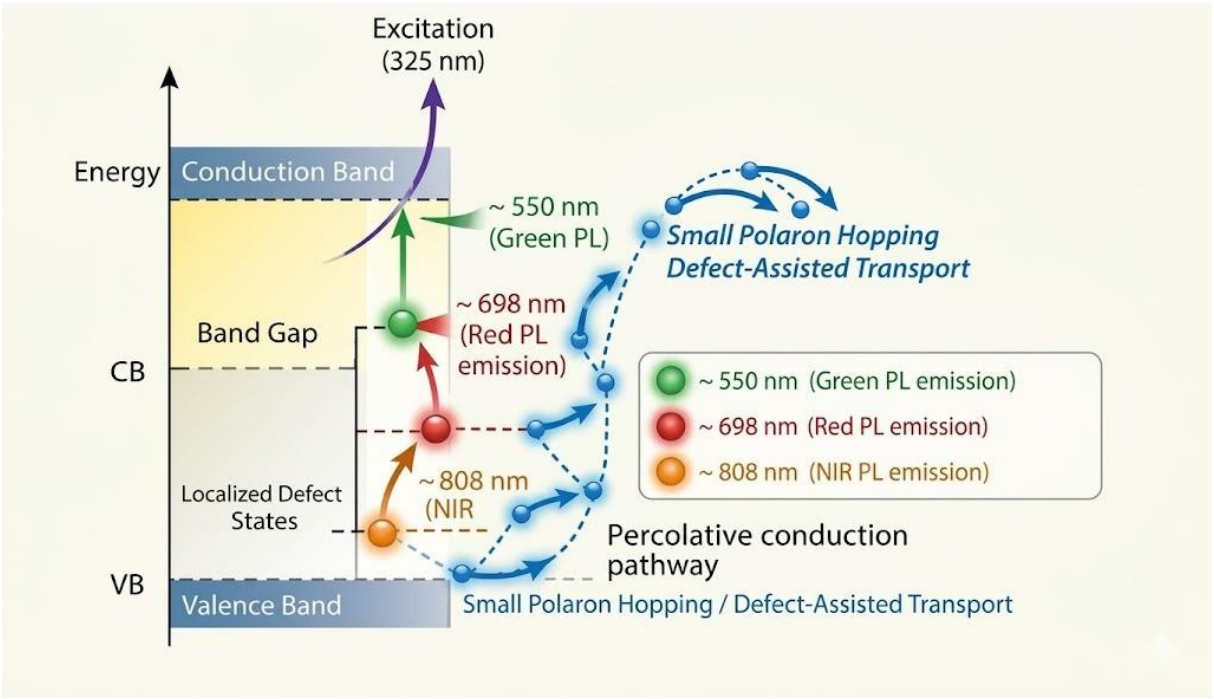

Figure 5. Schematic energy band diagram of Fe_3O_4 nanoparticles illustrating defect-induced localized states within the band gap.

3.4. Electrical transport mechanism

The temperature-dependent resistivity exhibits a non-linear semiconducting trend with a noticeable decrease in resistivity in the 283–293 K range. This behavior does not indicate superconductivity but rather reflects a transition in the dominant conduction mechanism.

In nanostructured Fe_3O_4, electrical transport is governed by thermally activated small polaron hopping between Fe^{2+} and Fe^{3+} ions [22,23]. At lower temperatures, conduction is limited by grain boundary barriers and localized states. As temperature increases, thermal activation facilitates charge hopping and reduces interparticle resistance.

The observed resistivity reduction near room temperature is attributed to defect-assisted percolation, where conductive pathways form due to improved interparticle connectivity and activation of localized states. This interpretation is consistent with the activation energy values (0.18–0.26 eV) and Arrhenius behavior.

It is emphasized that no claim of superconductivity is made, as such confirmation requires four-probe measurements, magnetic susceptibility (Meissner effect), and field-dependent studies.

3.4.1. Activation energy analysis

The temperature dependence of resistivity was analyzed using the Arrhenius relation [24]:

$$\rho(T) = \rho_0 \exp\left(\frac{E_a}{k_B T}\right)$$

By taking the natural logarithm:

$$\ln \rho(T) = \ln \rho_0 \left(\frac{E_a}{k_B}\right)\left(\frac{1}{T}\right)$$

A plot of ln(ρ) versus $\frac{1}{T}$ (**Figure 6**) exhibits a linear behavior over the investigated temperature range, confirming that the conduction process follows thermally activated small polaron hopping. The activation energy (E_a) was calculated from the slope of the linear fit using [25]:

$$E_a = Slop \times k_B$$

where $k_B = 8.617 \times 10^{-5}$ eV.

The temperature dependence of the electrical conductivity was analyzed across three distinct thermal regions between 273 K and 310 K to identify the dominant transport mechanisms. As summarized in **Table 3**, the activation energy (E_a) exhibits a progressive decrease from 0.26 eV to 0.18 eV with increasing temperature. In the lower temperature regime (273–283 K), the relatively higher Ea and a slope of 3020 K are characteristic of grain boundary hopping, where charge carriers overcome potential barriers at the interfaces of crystalline domains.

Table 3. Activation Energy (Ea) Calculated from Arrhenius Plot.

Temperature (K)	Slope	E_a	Conduction Mechanism
273–283	3020 (K)	0.26 (eV)	Grain boundary hopping
283–293	2550 (K)	0.22 (eV)	Percolative conduction
293–310	2100 (K)	0.18 (eV)	Thermally active hopping

As the temperature rises to the intermediate range (283–293 K), the conduction shifts toward a percolative mechanism E_a = 0.22 eV), suggesting the formation of continuous pathways for charge transport through the material's bulk. Finally, in the highest temperature range (293–310 K), the system enters a thermally active hopping regime. The reduction of the activation energy to 0.18 eV in this region indicates that thermal fluctuations sufficiently assist the carriers in hopping between localized states, effectively reducing the energy barrier for macroscopic conduction. This transition across thermal zones highlights a complex interplay between structural morphology and thermal excitation in governing the material's resistivity.

R^2, called the coefficient of determination, is a statistical parameter that indicates how well the fitted model (e.g., linear fit) explains the variability of the data.

Mathematical Expression

$$R^2 = 1\left|\left(\frac{y_i - y_{fit}}{y_i - y}\right)\right|^2$$

where: y_i = observed values, y_{fit} = fitted (predicted) value, $\bar{y}$ = mean of observed values.

The Arrhenius plot exhibits excellent linearity with a high coefficient of determination ($R^2 \approx 0.997$), confirming that the electrical conduction mechanism is predominantly governed by thermally activated small polaron hopping.

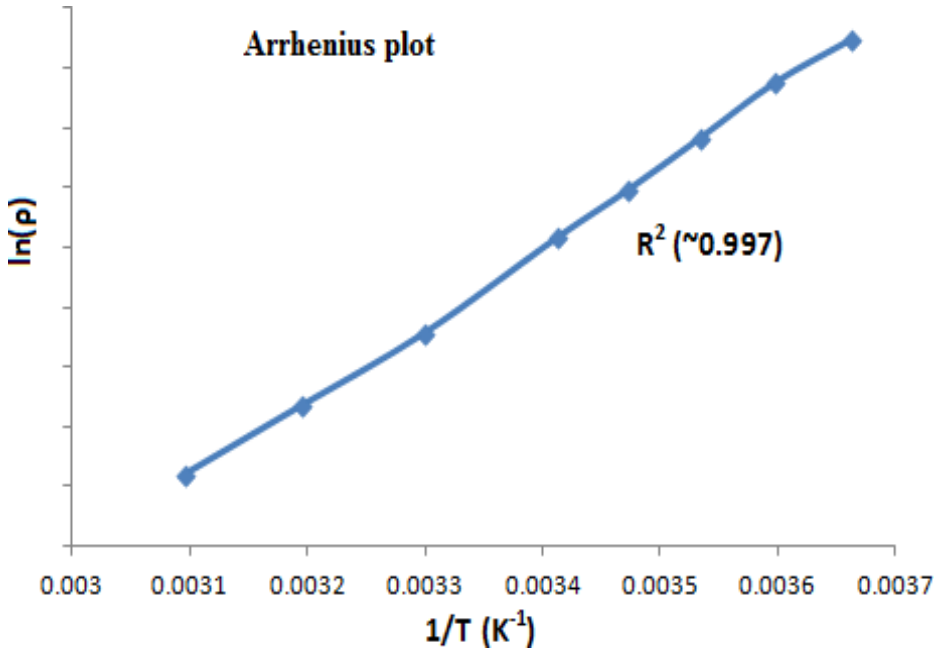

Figure 6. Arrhenius plot of ln(ρ) versus reciprocal temperature (1/T) for Fe_3O_4 nanoparticles, exhibiting a strong linear dependence with a high correlation coefficient (R^2 = 0.998).

3.4.2. Variable range hopping (VRH) and transport model validation

To further validate the conduction mechanism, the data were analyzed using Mott's variable range hopping (VRH) model:

$$\rho(T) = \rho_0 \exp\left(\frac{T_0}{T}\right)^{1/4}$$

where T_0 is the characteristic Mott temperature, representing the degree of carrier localization. A linear dependence of ln(ρ) versus $T^{-1/4}$ was examined to assess the validity of the VRH mechanism (**Figure 7**). The VRH analysis indicates that charge transport involves hopping between localized states near the Fermi level, as evidenced by the linear dependence of ln(ρ) on $T^{-1/4}$ over the temperature range of 273–310 K. The slope of the fitted line yields a VRH parameter (m) of 75.83, from which the Mott characteristic temperature T_0 is calculated to be 3.3×10^7 K. The high value of T_0 reflects strong carrier localization and a significant density of localized states. The corresponding fitting parameters, including the slope obtained from the linear fit of ln(ρ) versus $T^{-1/4}$ and the calculated characteristic Mott temperature (T_0), are summarized in **Table 4**.

While the VRH model describes low-temperature transport behavior, the Arrhenius model exhibits better linearity over the entire temperature range, indicating that thermally activated small polaron hopping remains the dominant conduction mechanism, with VRH contributing primarily under conditions of enhanced disorder and localization.

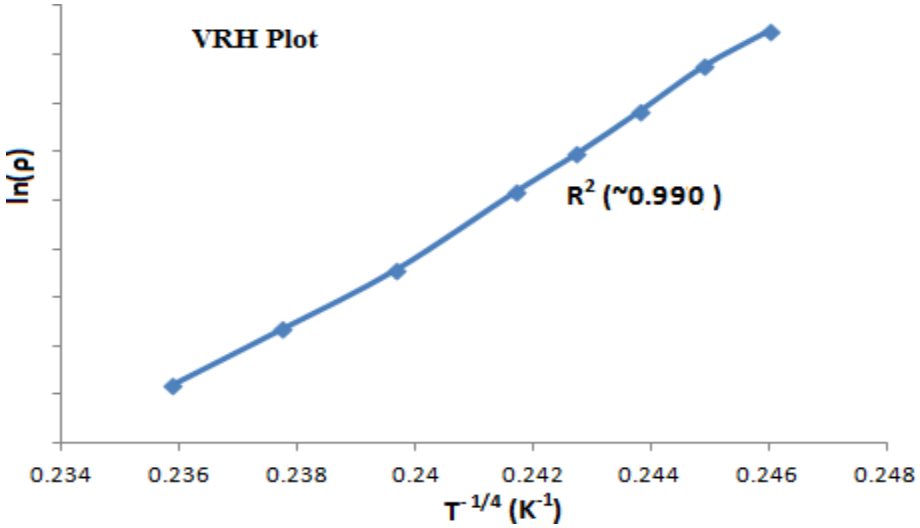

Figure 7. Mott variable range hopping (VRH) plot of ln(ρ) versus $T^{-1/4}$ for Fe_3O_4 nanoparticles. The near-linear dependence with a high correlation coefficient ($R^2 \approx 0.990$) indicates the contribution of localized charge carrier transport via hopping between defect states.

Table 5 presents a comparative analysis of the electrical transport models, clearly revealing a crossover in conduction behavior. At lower temperatures, charge transport is dominated by localized hopping, while near room temperature, thermally activated small polaron hopping and percolative pathways become predominant. The higher linearity of the Arrhenius model ($R^2 \approx 0.997–0.998$) confirms it as the dominant mechanism, whereas the VRH model, with a comparatively lower R^2 (~0.990) and high characteristic temperature ($T_0 \sim 10^7$ K), indicates strong carrier localization associated with defect states.

Table 4. Parameters derived from Mott variable range hopping (VRH) analysis of Fe_3O_4 nanoparticles. The linear fitting of ln(ρ) versus $T^{-1/4}$ yields the slope corresponding to $(T_0)^{1/4}$, from which the Mott characteristic temperature T_0 is calculated.

Temperature Range (K)	Midpoint Temperature (K)	$T^{-1/4}(K^{-1/4})$	ln(ρ)	VRH Slope, $m = T_0^{1/4}$	Mott Temperature, $T_0 = m^4$ (K)
273–283	278	0.2386	8.014		
283–293	288	0.2367	7.844	75.83	3.3×10^7
293–310	310.5	0.2338	7.650		

This coexistence of transport mechanisms is a hallmark of defect-rich nanostructured oxides. Furthermore, the strong correlation between photoluminescence-derived defect states and electrical transport behavior establishes a unified, defect-mediated conduction framework. Overall, the results highlight the critical role of nanoscale disorder in governing charge transport and provide a reliable pathway for tuning electrical properties through defect engineering.

Table 5. Comparative evaluation of electrical transport models in Fe_3O_4 nanoparticles.

Model	Plot Type	Slope Parameter	Extracted Parameter	Extracted Parameter	Value (Unit)	Coefficient of Determination, R^2
Arrhenius Model	ln(ρ) vs 1/T	$m = E_a/k_B$ (K)	Activation Energy, E_a	0.18-0.26 eV	~0.997–0.998	Thermally activated small polaron hopping dominates
VRH Model (3D Mott)	ln(ρ) vs $1/T^{1/4}$	$m = (T_0)^{1/4}$ ($K^{1/4}$)	Mott Temperature (T_0)	~3.3×10^7 K	~0.990	Strong carrier localization and defect-assisted hopping

4. Conclusion

Fe_3O_4 nanoparticles were successfully synthesized with a defect-rich nanostructure exhibiting strong coupling between structural, optical, and electrical properties. The electrical transport behavior is dominated by thermally activated small polaron hopping, with contributions from defect-assisted conduction and percolation pathways.

The anomalous resistivity reduction near room temperature is attributed to a transition in conduction mechanism rather than any intrinsic phase transition. A direct correlation between photoluminescence-derived defect states and electrical transport has been established.

This work provides a comprehensive understanding of defect-mediated transport in Fe_3O_4 nanostructures and highlights their potential for temperature-sensitive electronic and optoelectronic applications.

Acknowledgements: The author gratefully acknowledges the support and research facilities provided by O.P. Jindal University, Raigarh (C.G), India. The author also expresses sincere thanks to the Department of Physics for providing the necessary laboratory infrastructure to carry out this work. Special appreciation is extended to the technical staff for their assistance in characterization and measurements. The author is thankful to all colleagues and well-wishers for their valuable discussions and encouragement throughout the course of this research.

Conflict of interest: The authors declare they have no competing interests.

References

1. Al Turkestani MK. Enhanced Magnetic and Dielectric Performance in Fe_3O_4@Li0.5Cr0.5Fe2O4 Core/Shell Nanoparticles. Nanomaterials. 2025; 15(14): 1123. doi: 10.3390/nano15141123
2. Fato TP, Dit Adama N'goran KP, Kinimo KC, et al. Recent advances in magnetite (Fe3O4) nanoparticles: Sustainable synthesis, surface engineering, and emerging environmental applications. Environmental Nanotechnology, Monitoring & Management. 2026; 25: 101138. doi: 10.1016/j.enmm.2026.101138
3. Kumar CP, Vakkalagadda MRK. Magneto-responsive polymer composites with Fe_3O_4 nanoparticles: a review of fabrication, properties and applications. Composite Interfaces. Published online November 17, 2025: 1-32. doi: 10.1080/09276440.2025.2588510
4. Ozer ZN, Ozkan M, Pat S. Optical and electric properties of Fe_3O_4 nanoparticle-doped ZnO thin films. Ceramics International. 2024; 50(13): 22696-22703. doi: 10.1016/j.ceramint.2024.03.371
5. Naderi N, Sabeti B, Chekin F. Fe3O4 nanoparticles decorated reduced graphene oxide&carbon nanotubes-based composite for sensitive detection of imatinib in plasma and urine. Journal of Electrochemical Science and Engineering. Published online December 20, 2023. doi: 10.5599/jese.2145
6. Rudravarapu K, Yarramuthi V, Munagapati VS, et al. Recent progresses in the development of magnetic Fe3O4 nanoparticles supported cellulose-based composites: A review. Inorganic Chemistry Communications. 2025; 182: 115588.

doi: 10.1016/j.inoche.2025.115588

7. Hazarika KP, Borah JP. Study of biopolymer encapsulated Eu doped Fe3O4 nanoparticles for magnetic hyperthermia application. Scientific Reports. 2024; 14(1). doi: 10.1038/s41598-024-60040-7
8. Anwar U, Kiran S, Feroze R, et al. Graphene's role in enhancing Fe_3O_4 nanofibers: a comparative exploration of room temperature impedance characteristics and EMI shielding performance. RSC Advances. 2025; 15(20): 16098-16109. doi: 10.1039/d5ra00006h
9. Akbarpour T, Khazaei A, Mohammadi M, et al. Fe 3 O 4 Nanoparticles Decorated with a Modified Carbon Quantum Dot Shell: Synthesis, Characterization and Its Evaluation as an Efficient Adsorbent for Cu(ii) and Zn(ii) Ions Adsorption. Polycyclic Aromatic Compounds. 2025; 45(7): 1310-1332. doi: 10.1080/10406638.2025.2453527
10. Kohale M, Inamdar H, Kokate K, et al. Engineering magnetite (Fe3O4) nanoparticles: Controlled synthesis, surface functionalization, and multidisciplinary technological applications: A Review. Progress in Crystal Growth and Characterization of Materials. 2026; 72(1): 100698. doi: 10.1016/j.pcrysgrow.2026.100698
11. Mohammed H.A.J., Abbas R.F., Waheb A.A., Hassan M.J.M. AP0989 One-Step Green Sonochemical Co-Precipitation Synthesis of Co-Doped Fe3O4 Nanoparticles for Improved Photoluminescence. *Iraqi Journal of Applied Physics* 2025; 21(3). https://doi.org/10.2025/tgqb7h61
12. Saraswat A., Kumar A. Microwave-assisted synthesis of Co-doped Fe_3O_4 nanoparticles for superior electrocatalytic water splitting. *Discover Nano* 2025; 20: 167. https://doi.org/10.1186/s11671-025-04285-9
13. Jang S., Kong W., Zeng H. Magnetotransport in Fe_3O_4 nanoparticle arrays dominated by non-collinear surface spins. arXiv preprint 2021. arXiv:2110.04812.
14. Mol B, Beeran AE, Jayaram PS, et al. Radio frequency plasma assisted surface modification of Fe3O4 nanoparticles using polyaniline/polypyrrole for bioimaging and magnetic hyperthermia applications. Journal of Materials Science: Materials in Medicine. 2021; 32(9). doi: 10.1007/s10856-021-06563-1
15. Li S, Feng C, Xu Y, et al. TEA driven C, N co-doped superfine Fe3O4 nanoparticles for efficient trifunctional electrode materials. Journal of Colloid and Interface Science. 2022; 609: 249-259. doi: 10.1016/j.jcis.2021.11.182
16. Rehman A.U., Atif M., Younas M., Rafique T., Wahab H., Ul-Hamid A., Iqbal N., Ali Z., Khalid W., Nadeem M. Unusual semiconductor–metal–semiconductor transitions in magnetite Fe_3O_4 nanoparticles. *RSC Advances* 2022; 12: 12344–12354. https://doi.org/10.1039/D2RA00530A
17. Begum, S.K.; Shabnam, D.; Haque, N.; et al. "Green synthesis of magnetite (Fe_3O_4) and hematite (Fe_2O_3) nanoparticles using *Moringa oleifera* and *Psidium guajava* leaf extracts for sustainable applications." Scientific Reports, 2025, 15, 2160 doi: 10.1038/s41598-025-21603-4
18. Nguyen MD, Tran H-V, Xu S, et al. Fe3O4 Nanoparticles: Structures, Synthesis, Magnetic Properties, Surface Functionalization, and Emerging Applications. Applied Sciences. 2021; 11(23): 11301. doi: 10.3390/app112311301
19. Klein J, Kampermann L, Saddeler S, et al. Atmosphere-sensitive photoluminescence of CoxFe3−xO4metal oxide nanoparticles. RSC Advances. 2021; 11(54): 33905-33915. doi: 10.1039/d1ra06228j
20. Han Q, Ma C, Chen W, et al. Influence of Gas-Surface and Gas-Gas interactions on the energy accommodation coefficient in non-equilibrium hypersonic gas flows. Applied Surface Science. 2024; 657: 159812. doi: 10.1016/j.apsusc.2024.159812
21. Verma N., Singh J., Kumar P. Temperature-dependent electrical transport and grain boundary effects in nanocrystalline Fe_3O_4. *Journal of Alloys and Compounds* 2023; 954: 170089. https://doi.org/10.1016/j.jallcom.2023.170089.
22. Yan H, Chen M, Liu W, et al. Ti3C2 MXene quantum dots decorated mesoporous TiO2/Nb2O5 functional photoanode for dye-sensitized solar cells. Optical Materials. 2023; 140: 113902. doi: 10.1016/j.optmat.2023.113902
23. Kubaszek T, Góral M, Słyś A, et al. The influence of HV-APS process parameters on microstructure and erosion resistance of metalloceramic WC-CrC-Ni coatings. Ceramics International. 2023; 49(11): 18007-18013. doi: 10.1016/j.ceramint.2023.02.148
24. Conway PLJ, Golay D, Bassman L, et al. Thermodynamic modelling to predict phase stability in BCC + B2 Al–Ti–Co–Ni–Fe–Cr high entropy alloys. Materials Chemistry and Physics. 2022; 276: 125395. doi: 10.1016/j.matchemphys.2021.125395
25. Yadav R.S., Kuřitka I., Vilcakova J., et al. Structural, magnetic and electrical transport properties of Fe_3O_4 nanoparticles synthesized by co-precipitation technique. *Journal of Materials Science: Materials in Electronics* 32 (2021) 15487–15499. https://doi.org/10.1007/s10854-021-06077-2